Kinetic effects on neutron generation in moderately collisional interpenetrating plasma flows

D. P. Higginson (ID), J. S. Ross, D. D. Ryutov (ID), F. Fiuza (ID), S. C. Wilks, E. P. Hartouni (ID), R. Hatarik, C. M. Huntington (ID), J. Kilkenny, B. Lahmann (ID), C. K. Li, A. Link, R. D. Petrasso (ID), B. B. Pollock, B. A. Remington (ID), H. G. Rinderknecht (ID), Y. Sakawa (ID), H. Sio (ID), G. F. Swadling (ID), S. Weber, A. B. Zylstra (ID), and H.-S. Park

View Online

Export Citation

CrossMark

ARTICLES YOU MAY BE INTERESTED IN

Observation of collisionless-to-collisional transition in colliding plasma jets with optical Thomson scattering
Physics of Plasmas **26**, 012101 (2019); https://doi.org/10.1063/1.5047218

High-order two-fluid plasma solver for direct numerical simulations of plasma flows with full transport phenomena
Physics of Plasmas **26**, 012109 (2019); https://doi.org/10.1063/1.5082190

Scaling laws for dynamical plasma phenomena
Physics of Plasmas **25**, 100501 (2018); https://doi.org/10.1063/1.5042254

Kinetic effects on neutron generation in moderately collisional interpenetrating plasma flows

View Online   Export Citation   CrossMark

D. P. Higginson,[1,a] [iD] J. S. Ross,[1] D. D. Ryutov,[1] [iD] F. Fiuza,[1,2] [iD] S. C. Wilks,[1] E. P. Hartouni,[1] [iD] R. Hatarik,[1]
C. M. Huntington,[1] [iD] J. Kilkenny,[3] B. Lahmann,[4] [iD] C. K. Li,[4] A. Link,[1] R. D. Petrasso,[4] [iD] B. B. Pollock,[1]
B. A. Remington,[1] [iD] H. G. Rinderknecht,[1,b] [iD] Y. Sakawa,[5] [iD] H. Sio,[4] G. F. Swadling,[1] [iD] S. Weber,[1]
A. B. Zylstra,[1,6] [iD] and H.-S. Park[1]

AFFILIATIONS

[1] Lawrence Livermore National Laboratory, P.O. Box 808, Livermore, California 94551, USA
[2] SLAC National Accelerator Laboratory, Stanford University, Stanford, California 94305, USA
[3] General Atomics, San Diego, California 92121, USA
[4] Massachusetts Institute of Technology, Cambridge, Massachusetts 02139, USA
[5] Institute of Laser Engineering, Osaka University, 2-6 Yamadaoka, Suita 565-0871, Japan
[6] Los Alamos National Laboratory, Los Alamos, New Mexico 87545, USA

[a] Author to whom correspondence should be addressed: higginson2@llnl.gov
[b] Also at: Laboratory for Laser Energetics, University of Rochester, Rochester, New York 14623, USA

ABSTRACT

Collisional kinetic modifications of ion distributions in interpenetrating flows are investigated by irradiating two opposing targets, either CD/CD or CD/CH, on the National Ignition Facility. In the CD/CD case, neutron time-of-flight diagnostics are successfully used to infer the ion temperature, 5–6 keV, and velocity, 500 km/s per flow, of the flows using a multi-fluid approximation of beam-beam nuclear fusion. These values are found to be in agreement with simulations and other diagnostics. However, for CD/CH, the multi-fluid assumption breaks down, as fusion is quasi-thermonuclear in this case and thus more dependent on the details of the ion velocity distribution. Using kinetic-ion, hydrodynamic-electron, and hybrid particle-in-cell modeling, this is found to be partially due to a skewed deviation from a Maxwellian in the ion velocity distribution function resulting from ion-ion collisions. This skew causes a downshift in the mean neutron velocity that partially resolves the observation in the CD/CH case. We note that the discrepancy is not completely resolved via collisional effects alone and may be a signature of collisionless electromagnetic interactions such as the Weibel-filamentation instability.

I. INTRODUCTION

Interpenetration is present in many plasma systems, from astrophysics to inertial confinement fusion. It occurs when flows intersect at low enough density and high enough velocity such that the length of the Coulomb mean-free-path, λ, is on the order of or greater than, the region of interest, L. The mean-free-path is strongly dependent on the ion density, n_i and relative velocity, v_{rel}, which is given as follows:

$$\lambda = 4\pi\epsilon_0^2 m_r^2 v_{rel}^4/(q_i^2 q_j^2 n_i \ln \Lambda), \qquad (1)$$

where ϵ_0 is the vacuum permittivity, m_r is the reduced mass, q is the ion charge, and $\ln \Lambda$ is the Coulomb logarithm. In astrophysical systems, such as supernova remnant shocks, λ can be hundreds of times greater than the width of shock,[1–3] meaning that collisions can be neglected entirely. In this $\lambda \gg L$ regime, the dynamics are dominated by long-range, collective electromagnetic (EM) forces, such as the Weibel-filamentation instability[4] that can create EM instabilities and potentially collisionless shocks. Using appropriate scaling relations,[5–7] such astrophysical scenarios can be studied in the laboratory using high-energy lasers; this is currently an active area of research experimentally,[3,8–12] theoretically,[6,13] and computationally.[14–17] On the other hand, laser-driven inertial

confinement fusion (ICF) experiments often occur at high density such that the plasma is very collisional and λ is small. In this $\lambda \ll L$ regime, the plasma cannot interpenetrate, ions will be in local thermal equilibrium, a Maxwellian description is justified, and single-fluid, radiation hydrodynamic (RH) codes are expected to be valid. However, such ICF systems are dynamic, and conditions where $\lambda \geq L$ occur at various locations in space and time.[18] For instance, interpenetration may occur between the hohlraum-wall, gas-fill, and capsule-ablator in low gas fill hohlraums leading to higher than expected laser transmission as compared to RH simulations[19–21] and separation of ion species may be responsible for yield anomalies in laser-driven capsule implosions.[22–24] Other laser driven neutron generation schemes, such as those related to converging plasma flows,[25–29] may include both thermonuclear (i.e., $\lambda \leq L$) and beam-beam (i.e., $\lambda \geq L$) fusion reactions; an understanding of this is necessary to accurately predict the yield on larger systems.

The regime of interest of this work is $\lambda \sim L$. Here, collisional interactions are important yet ions are not necessarily in thermodynamic equilibrium with each other and a Maxwellian description may not be valid. In this regime, resolution of the distribution function of the particles may be important, for instance due to the variation of the Rutherford scattering cross-section with particle velocity. There has been a broad history of the study of this regime of plasma interaction on high-energy laser systems.[30–35] In these experiments, two foils are placed opposite to each other and irradiated on their facing sides so that the two relatively high-electron-density ($n_e \sim 10^{20}\,\mathrm{cm}^{-3}$), relatively high-velocity (500–1000 km/s) plasmas flow into each other. This work showed that a single-fluid approach was invalid due to the inability to capture the interpenetration of the flows. Still, the general consensus, stemming from the comparison between multi-fluid and fully kinetic particle-in-cell (PIC) simulations, was that in these systems, the multi-fluid approach was valid within 10%–20%, meaning that bulk quantities such as temperatures, velocities, and densities were similar in both approaches. In general, however, there are many plasma properties (e.g., heat transport, magnetic field advection, neutron production) that depend not only on bulk plasma properties, but also on the specific form of the distribution function in the plasma.

In this article, we explore the importance of details in the ion distribution functions of interpenetrating plasmas on neutron generation, via both experiment and simulation. We study temporally evolving, moderately collisional systems where the mean-free-path, $\lambda = 0.1$–10 mm, is on the order of the system size, $L = 6$ mm. In this regime, we find that non-Maxwellian skewing of the ion distribution function caused by ion-ion collisional effects results in large changes to the yield and energy spectra of DD fusion generated neutrons.

II. EXPERIMENTAL SETUP AND RESULTS

A. Experimental setup description

The experiment was performed on the National Ignition Facility (NIF) by irradiating foil targets placed opposite to each other so that the laser-ablation created two counter streaming, interpenetrating plasma flows, as shown in Fig. 1. The CD and CH foils were positioned 3 mm from the target chamber center.
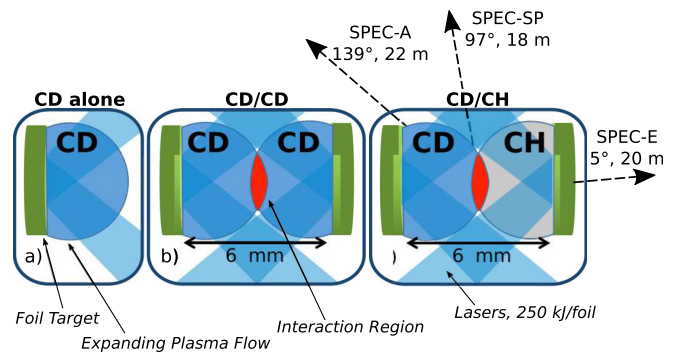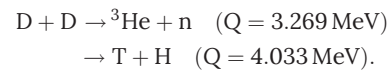

FIG. 1. The three target configurations used on NIF; each foil is irradiated with 250 kJ of laser energy. (a) Single CD foil; neutron yield is thermonuclear from the laser-target heating, (b) CD/CD; neutron yield is dominated by beam-beam DD neutrons, (c) CD/CH; yield is created by heating the incoming deuteron stream by the CH stream. The dotted lines indicate the location of the NTOF diagnostics with diagnostic descriptors (e.g., SPEC-A), angle with respect to the CD flow, and distance from the center of the foils indicated; these are the same for every setup.

Each foil was 2.5 mm in diameter and 0.5 mm in thickness. The foils were each irradiated with forty-eight, 351 nm laser beams. Each beam delivers 5.2 kJ in a 5 ns square pulse, resulting in a total of around 250 kJ per foil. The beams used continuous phase plates to produce supergaussian focal spots with a supergaussian exponent of 4.3 and a diameter of 1200 μm. This resulted in an overlapped laser intensity of $2.8 \times 10^{15}\,\mathrm{W/cm}^2$ on each foil.

As the foils contained deuterium, fusion products were generated via DD reactions

$$\mathrm{D} + \mathrm{D} \rightarrow {}^3\mathrm{He} + \mathrm{n} \quad (Q = 3.269\,\mathrm{MeV})$$
$$\rightarrow \mathrm{T} + \mathrm{H} \quad (Q = 4.033\,\mathrm{MeV}).$$

In the limit of zero deuteron kinetic energy, neutrons from the d(D,^{3}He)n reaction are born with a neutron energy, $\mathcal{E}_n$, of 2.45 MeV. As the relative kinetic energy of the deuterons increases so does the energy of the produced neutrons. Also, a finite center-of-mass velocity, $\mathbf{v}_{cm}$, creates an upshift in neutron energy in the positive $\mathbf{v}_{cm}$ direction and a downshift in the negative $\mathbf{v}_{cm}$ direction. Such characteristics make the measurement of DD fusion neutrons an informative tool to understand the deuteron flow parameters.

Three different target configurations were used in the experiment to investigate the interaction via neutron diagnostics. The first setup used a single CD foil [Fig. 1(a)]. Since the laser-target interaction creates a dense plasma that is heated to high (few keV) temperatures by the laser, this configuration produces a background of thermonuclear neutrons near the target surface, neutrons which are unrelated to the interaction between the two plasma flows of interest to this study. This background is subtracted from the two-foil interaction cases. The second case [CD/CD: Fig. 1(b)] used two symmetrically placed CD foils; here the majority of neutrons are produced by the head-on beam-beam interactions between deuterons of opposing flows. The third case [CD/CH: Fig. 1(c)] used a CD and a CH foil. In this case, neutrons are produced by DD fusion reactions in the CD flow.

These deuterons are heated by interactions (e.g., collisions, EM instabilities) with the opposing flow.

B. Experimental results

To diagnose the neutron production, neutron time-of-flight spectrometers (NTOFs) were located at different angles relative to the two targets as shown in Fig. 1. Angles are defined with respect to the CD flow in all setups; thus, in the CD/CH case, the CD flows towards 0° and the CH flows towards 180°. The NTOFs were placed from 18 to 22 m from the chamber center and therefore, the dispersion in time is dominated by the time-of-flight broadening due to the breadth of the neutron energy spectrum and not the, few ns, neutron burn duration. Details of the NTOF detectors can be found in Refs. 36–39 and Appendix A. The average yields of the NTOFs are shown in Table I. We see that each case is separated from the others by at least a factor of 10. This means that we can separate the mechanisms that produce neutrons in each individual case. Since the CD alone case is at most 10% of the total yield of the others, we can neglect the yield arising from laser-target interactions in the other cases. As the CD/CH case has a yield of around 10 times less than that of CD/CD, we expect that almost all of the yield in the CD/CD case is due to beam-beam interactions and not from interactions due to heating within the individual beams. In addition to the NTOFs, a particle time-of-flight (PTOF) detector was fielded.[40] This detector is similar in principle to the NTOFs except that it is placed at a distance of only 0.5 m from the targets and therefore is relatively insensitive to time-of-flight broadening; this means that this detector is measuring the peak time of the neutron production. To get a rough first estimate of the flow speed, we assume that the flows arrive at the mid-point between of the two foils (i.e., 3 mm from the target) at the neutron peak time. This gives rough velocities of 545 km/s and 525 km/s in the CD/CD and CD/CH cases, respectively.

To get a better understanding of the flow velocities and temperatures, we look in detail at the neutron spectra from the NTOFs at each angle for the CD/CD and CD/CH cases in Fig. 2. As we are interested in understanding only the neutrons generated from the interaction between the two flows, we subtract the CD alone NTOF signal from the CD/CH and the CD/CD cases, first multiplying the CD alone by two in the CD/CD case to account for the two foils. The resulting signals after subtraction are plotted in Fig. 2 for the two cases at the three different angles in the experiment. The time scale in the figure has been shifted so that $t = 0$ corresponds to the time that a neutron generated at the moment of peak nuclear burn (~5.5 ns from the PTOF) from a cold, stationary plasma ($\mathcal{E}_n = 2.45$ MeV) would reach the detector. Thus, in the plot, negative times correspond
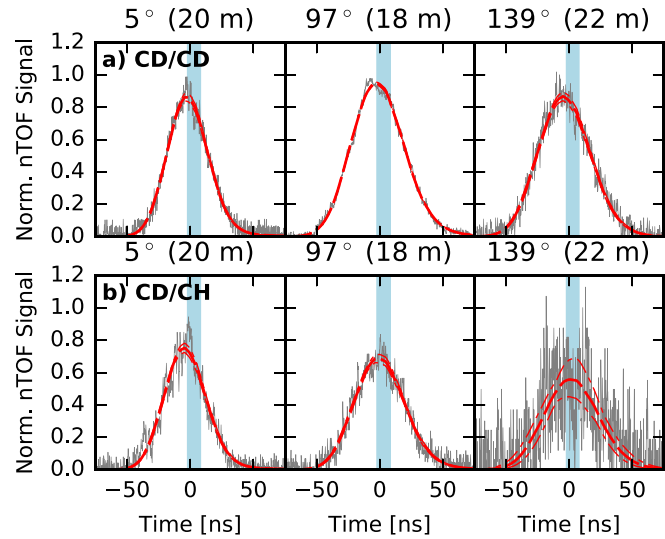

FIG. 2. Neutron time-of-flight signals (solid lines), for (a) the CD/CD and (b) the CD/CH case for three detector locations. Best fits with a Gaussian distribution function are shown as dashed lines with error bars represented as thinner dashed-dotted lines. The light background bar represents 10% temporal broadening from the detector response.

to neutrons with kinetic energies higher than 2.45 MeV and those that arrive at positive times are lower than 2.45 MeV. The light-shaded region in Fig. 2 represents the temporal spreading of the detector as defined as 10% of the peak (see Appendix A).

In the NTOF signals in Fig. 2(a) in the CD/CD case, the measured neutron energies are isotropically upshifted, as reflected in the peak being slightly shifted to times less than $t = 0$, meaning that these neutrons arrive earlier in time than expected for a cold plasma. This is consistent with addition of energy into the center-of-mass frame for the reaction. In the CD/CH case shown in Fig. 2(b), the neutron peaks show a shift that is dependent on the angle of observation. The highest energy up-shift is at 5° and this energy decreases as the observation angle increases. The direction of this shift is consistent with a Doppler shift along the direction of the CD flow. In addition to the shift of the neutron peaks, there are clear differences in the widths of the neutron spectra. Part of this broadening is due to the different distances of the detectors, as detectors further away will have broader signals. To quantify the neutron spectra, we use a shifted Gaussian spectrum, $g_n(\mathcal{E}_n)$, as follows:

$$g_n(\mathcal{E}_n) = N_y \left(2\pi\sigma_n^2\right)^{-1/2} \exp\left[-(\mathcal{E}_n - \mathcal{E}_s)^2/(2\sigma_n^2)\right], \quad (2)$$

where $\mathcal{E}_n$ is the neutron energy, N_y is the total neutron yield, σ_n is the width, and $\mathcal{E}_s$ is the mean neutron energy. This function is converted into a temporal distribution at a given distance, and then multiplied by the temporal and energy dependent response of the detector to produce a synthetic signal. The parameters of $g_n(\mathcal{E}_n)$ are varied to get the best fit to the experimental data and the covariance is used as the uncertainty of the fit. We plot the best fits and uncertainty, along with the data, in Fig. 2.

TABLE I. Total neutron yield averaged over the 3 NTOFs and arrival time of the peak maximum neutron emission from the PTOF detector. The lack of a peak time in the CD alone case is due to low signal on that shot.

	CD/CD	CD/CH	CD Alone
Neutron yield	5.3×10^{10}	6.3×10^9	4.7×10^8
Peak time	5.5 ns	5.7 ns	Low signal

Often, for instance in a collisional, thermonuclear scenario, the width of the neutron spectrum is used to infer a temperature of the ions, assuming a relatively cold, thermal plasma with no macroscopic velocity motion.[41,42] As this width may be broadened via other mechanisms, we call this the "apparent" ion temperature, T_{app}, which is given by

$$T_{app} \equiv \frac{(\hat{m}_n + \hat{m}_4)^2}{2\hat{m}_n \hat{m}_4 Q} \sigma_n^2 \overset{DD}{\simeq} \frac{\sigma_n^2}{1228\,keV}, \tag{3}$$

where $\hat{m}_n$ and $\hat{m}_4$ are the rest-mass energies (i.e., $\hat{m} = mc^2$, c is the speed of light) for the neutron and ^{3}He particle, respectively, and Q is the Q-value of the reaction. We use Eq. (3) to plot the apparent temperature for these interacting plasmas in Fig. 3. The results show that the NTOF spectral width is highest for the detector located at 97° relative to the direction of the plasma flow. Variation in the flow velocity over the volume where neutrons are produced will increase the neutron width along the different lines-of-sight. We extend the model of Murphy[43] to capture variable flow velocities in the radial, R, and longitudinal, Z, directions

$$\sigma_n^2 = \sigma_0^2 \cos^2\theta + \sigma_{90}^2 \sin^2\theta, \tag{4}$$

where $\sigma_0^2 = \sigma_{th}^2 + \sigma_Z^2$, $\sigma_{90}^2 = \sigma_{th}^2 + \sigma_R^2$ and θ is the angle with respect to the flow direction. The term σ_{th} is the broadening due to the temperature of the plasma and

$$\sigma_R^2 = \hat{m}_n^2 V_0^2 \langle v_R^2 \rangle c^{-4}, \quad \sigma_Z^2 = \hat{m}_n^2 V_0^2 \langle v_Z^2 \rangle c^{-4}$$

are broadening due to flow velocity fluctuations in the R and Z-directions, with $\sqrt{\langle v_R^2 \rangle}$, $\sqrt{\langle v_Z^2 \rangle}$ being the root-mean-squared (rms) flow velocities of the ions in the R and Z directions. We plot the best the fit of Eq. (4) to the data as a dashed curve in Fig. 3. Unfortunately, this fit does not allow us to uniquely determine the temperature of the ions due to the unknown contributions of broadening from flow fluctuations in the R and Z directions. Thus, from this fit, the most we can say is that the maximum isotropic ion temperature, $T_{max} = T_0$, is 5.5 keV and 5.9 keV for the CD/CD and CD/CH cases, respectively.

To understand the velocity of the flow, we consider the shift of the peak energy of the neutrons as a function of angle.
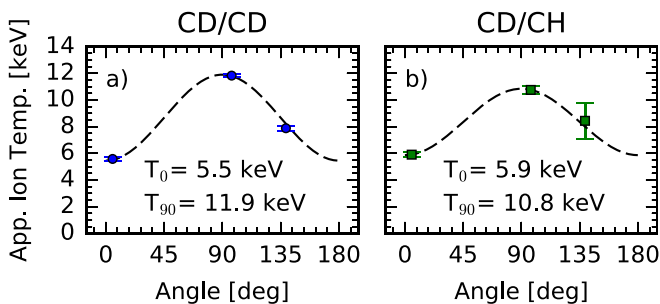

FIG. 3. Apparent ion temperature in (a) the CD/CD and (b) the CD/CH case as a function of detector angle relative to the plasma flow direction. Here, 0° corresponds to the direction of the CD flow as shown in Fig. 1. The dashed line indicates the best fit to the experimental data using Eq. (4): $T(\theta) = T_0 \cos^2\theta + T_{90} \sin^2\theta$, where we use units of apparent temperature from Eq. (3), e.g., $T_0 \simeq \sigma_0^2/1288\,keV$. For the CD/CD case, the best fits correspond to T_0 and T_{90} of 5.5 and 11.9 keV, respectively, and in the CD/CH case to 5.9 and 10.8 keV.

We transform the mean energy of the neutrons, $\mathcal{E}_s$, into the neutron mean velocity

$$V_n = c\sqrt{2\mathcal{E}_s/\hat{m}_n} \tag{5}$$

and define the velocity shift, ΔV_n, as

$$\Delta V_n = V_n - V_0, \tag{6}$$

where $V_0 \simeq 21.65 \times 10^3$ km/s corresponds to the kinetic energy of a neutron created from a cold, stationary deuterium plasma. For clarity, to describe velocities we use uppercase, V, for neutrons and lowercase, v, for deuterons.

The mean neutron velocity shifts are shown in Fig. 4 for the different cases as a function of observation angle. As observed in the raw NTOF signals, it is clear that neutrons are isotropically up-shifted in energy in the CD/CD case and that an angular Doppler-like shift towards the direction of the CD flow is observed in the CD/CH case. This is understood using a simple two-particle kinematics equation

$$\Delta V_n \simeq u_{cm} \cos\theta + \frac{1}{2V_0}\frac{\hat{m}_r}{\hat{m}_\star} u_{rel}^2, \tag{7}$$

where $\hat{m}_r = \hat{m}_1 \hat{m}_2 / (\hat{m}_1 + \hat{m}_2)$ is the reduced mass, $\hat{m}_\star = (\hat{m}_n/\hat{m}_4)(\hat{m}_n + \hat{m}_4)$, and u_{rel} and u_{cm} are, respectively, the relative and center-of-mass velocities between the two particles. Here, we use a lowercase u to represent velocities associated with this two-particle model. We note that this equation is simplified assuming $V_0 \gg u_{cm}$ and $V_0 \gg u_{rel}$. The derivation of this equation and its unsimplified version are shown in Appendix B1. Equation (7) is consistent with the observations in the data: in the CD/CD case, there is an up-shift in velocity due to the relative velocity of the two flows and there is no angular variation of the velocity, as the neutrons are produced by beam-beam interactions between the two flows; thus, as the flows are symmetric, there is no average center-of-mass velocity; and in the CD/CH case we observe an angular dependence of velocity given that neutrons are produced in the CD plasma flow with a given flow velocity and thus a center-of-mass velocity. We show the fits of the data in Table II for both cases.

Equation (7) is a binary kinematic relationship describing the interaction of two individual ions without taking into

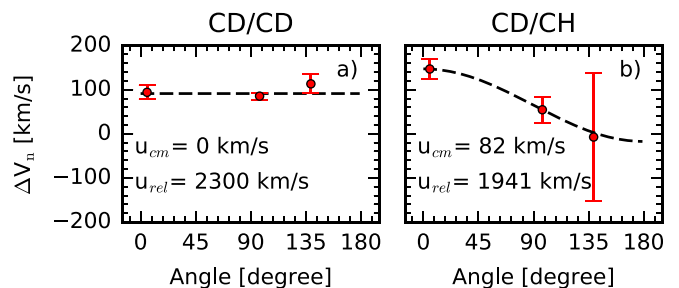**FIG. 4.** Mean neutron velocity shift in (a) the CD/CD and (b) the CD/CH case as a function of detector angle, where 0° is the direction of the CD flow as shown in Fig. 1. The dashed line indicates the best fit to the data using the two-particle kinematics Eq. (7). Here, u_{rel} and u_{cm} are the relative and center of mass velocities, respectively, for the two-particle fit with best fit parameters shown on the graphs.

TABLE II. Results of the fits to the data using the two-particle model from (7), where u_{rel} is the relative velocity and u_{cm} is the center-of-mass velocity. In the CD/CD case, we assume symmetric opposing flows, Eq. (8), to solve for the flow velocity, v_f, via Eq. (9) using the maximum isotropic temperature, T_{max} estimated from the fit, Eq. (4), to the neutron width. In the CD/CH case we assume a single flow, Eq. (10) to solve for both flow velocity and temperature, T, of the flow using Eq. (11).

	u_{rel} (km/s)	u_{cm} (km/s)	v_f (km/s)	T (keV)	T_{max} (keV)
CD/CD	2300	0	470		5.5
CD/CH	1941	82	82	5.5	4.9

account the fact that neutrons are produced by flows of ions within a distribution function with finite width. Given the strong dependence of fusion cross-section magnitude on the relative velocity, we cannot simply say that the neutrons will be produced at the mean velocities of the flows. Instead, in keeping with our binary description, we assume that neutrons are produced by two ions at the peak neutron producing velocities (i.e., u_{rel}, u_{cm}). These velocities are found by taking a given ion distribution function and applying the velocity dependent fusion cross-section to identify the ions most responsible for neutron generation. Then these ions can be used in the binary relationship of Eq. (7) to connect the parameters of the flow to the neutrons produced.

For the CD/CD case, we assume that the ion flows are two symmetrical drifting Maxwellian fluids with equal and opposite drift velocities of $\pm \mathbf{v_f}$ and the same temperature, T. This case is described by the total ion distribution function f_{BB} that includes both ion flows

$$f_{BB}(\mathbf{v}) \propto \exp\left[-\frac{(\mathbf{v} - \mathbf{v_f})^2}{2Tc^2/\hat{m}_i}\right] + \exp\left[-\frac{(\mathbf{v} + \mathbf{v_f})^2}{2Tc^2/\hat{m}_i}\right]. \quad (8)$$

Applying the fusion cross-section to identify the peak neutron producing ions (see Appendix B 3), we find that in a beam-beam case the peak center-of-mass velocity is zero ($u_{cm} = 0$) and the peak relative velocity, u_{rel}, is related to the flow velocity, by

$$\text{Beam-Beam}: \quad v_f = \frac{1}{2}\left(u_{rel} - \frac{2Tc^2 v_G}{\hat{m}_i u_{rel}^2}\right), \quad (9)$$

where $v_G = 2\pi c \alpha_f Z_1 Z_2$ is the velocity associated with the Gamow cross-section, α_f being the fine structure constant and Z being the charge state of the reactants. Equation (9) shows that u_{rel} is determined by both the flow velocity and the temperature. In the limit that the temperature is zero, we recover $u_{rel} = 2v_f$. In the limit that the flow velocity is zero, we recover the classical Gamow peak. Connecting this to the neutron velocity shift from Eq. (7) allows us to fit the data in the CD/CD case with a value of $u_{rel} = 2300$ km/s; this fit is plotted as a dashed curve in Fig. 4(a). Using the minimum temperature of 5.45 keV from the width of the NTOF (shown in Fig. 3), we find a velocity of the flow of $\sim$470 km/s. We note that this is a minimum for the velocity, and, for instance, if the temperature was only 5.0 keV, the inferred velocity would be 530 km/s. This value, around 500 km/s, is consistent with the flow velocities inferred from PTOF arrival time in both the CD/CD and CD/CH cases.

To evaluate the CD/CH case, we describe the ion distribution as a single, drifting Maxwellian, f_{TN}

$$f_{TN}(\mathbf{v}) \propto \exp\left[-\frac{(\mathbf{v} - \mathbf{v_f})^2}{2Tc^2/\hat{m}_i}\right]. \quad (10)$$

The velocity dependent cross-section is applied to this distribution and the peak neutron producing ions are found, as we show in detail in Appendix B 4. In this case, we find that the temperature is related to u_{rel}

$$\text{TN Drift}: \quad T = \hat{m}_i \frac{u_{rel}^3}{c^2 v_G} \quad (11)$$
$$v_f = u_{cm}$$

and the flow speed is related to u_{cm}. Using Eq. (7) allows us to fit the data in the CD/CH case with a value of $u_{rel} = 1941$ km/s and $u_{cm} = 82$ km/s; this fit is plotted as a dashed curve in Fig. 4(b). Using Eq. (11) indicates a temperature, T, of 5.5 keV with a flow velocity, v_f, of $\sim$82 km/s, which is a factor of 5.8 times smaller than the CD/CD case. This velocity is unreasonably low; it does not agree with either the PTOF measurements ($\sim$500 km/s) or the CD/CD case ($\sim$500 km/s), which should have a similar velocity profile. Additionally, using the inferred temperature of 5.5 keV, we can solve Eq. (4) for the rms velocity of the ions to get $\sqrt{\langle v_z^2 \rangle} = 93$ km/s and $\sqrt{\langle v_r^2 \rangle} = 355$ km/s. It does not seem plausible that the radial velocity variance can have a larger velocity than the flow itself. These multiple discrepancies are a clear indication that our fluid description found in Eq. (11) is not valid in this regime, likely due to the deviation of the plasma from a Maxwellian description.

To understand this fundamentally kinetic problem, we have run a particle-in-cell code with kinetic ion species including binary scattering and binary neutron production. This will show that the assumption of a Maxwellian plasma, as proposed by previous work,[30,33] was "correct" in the sense that it captures bulk plasma properties. However, neutron production is not dominated by ions in the bulk of the plasma, but instead by ions in the tails with kinetic energies a few times higher than the average kinetic energy. Thus, we will find that the small deviations in the tails of these distributions, as captured by kinetic ions, dramatically alter the produced neutron spectrum.

III. HYDRODYNAMIC PARTICLE-IN-CELL SIMULATIONS OF INTERPENETRATION AND NEUTRON GENERATION
A. Simulation description

The laser-plasma interaction was simulated with the radiation-hydrodynamics code HYDRA[44] using realistic laser pulses on a single foil. As HYDRA uses single-fluid hydrodynamics, ion densities were based on the initial distribution of ions in the solid target. The atomic density fractions were, for CH: 50.4% C and 49.6% H; and, for CD: 50.4% C, 40.5% D and 9.1% H. The code was run up to 3.5 ns after the beginning of the laser pulse at which time the spatially dependent plasma parameters (velocity, density, temperature) of both electrons and ions were recorded. At this time, the velocities were on the order of 1000 km/s, the electron density around 10^{20} cm^{-3}, and the ion (electron) temperature around 1 keV (2 keV) at the mid-point

between the two foils. These single foil parameters were truncated at the mid-plane (i.e., 3 mm from the target surface) and a secondary flow was created by flipping the single foil flow across the axis. These double flow parameters were then passed to the hydrodynamic particle-in-cell (hd-PIC) code Chicago.[45] The ion velocities (10% increase) and ion/electron densities (1.8× increase) were increased to match the yield and spectra in the CD/CD case. We discuss the sensitivity of our results to these multipliers in Appendix C. In the CD/CD case, nearly all neutrons are produced by beam-beam interactions and thus matching the neutron spectra is a good constraint on the initial conditions of the plasma. The need to increase the velocity is due to the fact that the hd-PIC simulations did not include the laser drive; thus, the final 1.5 ns of laser pulse was not available to accelerate the plasma.

The kinetic-ion, hydrodynamic-PIC formulation[45,46] used in Chicago follows the motion of kinetic ions, while modeling electrons with an Ohm's law. The derivation of this method, for the magnetized *fluid*-ion case, is found in Appendix A of Thoma *et al.*[45] We summarize this method for an *unmagnetized kinetic*-ion case, neglecting thermoelectric effects. To describe this method, we start with the particle push on a single kinetic ion k, from electric, $\mathbf{E}$, and magnetic, $\mathbf{B}$, fields and from scattering on electrons, C_{scat}^{ke}, and all other ions, C_{scat}^{ki}

$$m_k \frac{d\mathbf{v_k}}{dt} = e\bar{Z}_k(\mathbf{E} + \mathbf{v_k} \times \mathbf{B}) + C_{\text{scat}}^{ke} + C_{\text{scat}}^{ki}, \qquad (12)$$

where $\mathbf{v_k}$ is the velocity, m_k is the mass, $\bar{Z}_k$ is the charge state, and e is the elementary charge magnitude. To model an unmagnetized case, the magnetic field is neglected and the electric field is described through a generalized Ohm's Law

$$\mathbf{E} = -\frac{1}{en_e}\nabla P_e + \frac{m_e}{e}\sum_{j=1}^{N_{\text{ions}}}\nu_{ej}(\mathbf{v_j} - \mathbf{v_+}), \qquad (13)$$

where P_e is the electron pressure, $\mathbf{v_+}$ is the charge density weighted ion velocity

$$\mathbf{v_+} = \sum(\bar{Z}_j n_j/n_e)\mathbf{v_j}, \qquad (14)$$

and ν_{ej} is the collision frequency between electrons and the ion species j. Inserting this into the original push in (12) gives the push in the hd-PIC formulation

$$m_k \frac{d\mathbf{v_k}}{dt} = -\frac{\bar{Z}_k}{n_e}\nabla P_e + \bar{Z}_k m_e \sum_{j=1}^{N_{\text{ions}}}\nu_{ej}(\mathbf{v_j} - \mathbf{v_e})$$
$$-m_k\nu_{ke}(\mathbf{v_k} - \mathbf{v_+}) + C_{\text{scat}}^{ki}. \qquad (15)$$

Here, the ion-electron scattering (i.e., $m_k\nu_{ke}[\mathbf{v_k} - \mathbf{v_e}]$) is described via a fluid scattering model[34] with electrons traveling at the charged weighted velocity (i.e., $\mathbf{v_e} = \mathbf{v_+}$). Ion-ion scattering is described via binary collisions[47,48] with the inclusion of large-angle Rutherford scattering.[49] Densities and pressure gradients are gathered on the grid nodes and interpolated to the ion position during the particle advance. Electrons are modeled as a virtual species with attributes (i.e., velocity, temperature, density) carried by the ion particles. The electron temperature is advanced via fluid energy equations[50]

$$C_v \frac{dT_e}{dt} = -\frac{P_e}{n_e}\nabla \cdot \mathbf{v_e} + \frac{1}{n_e}\nabla \cdot (\kappa_e \nabla T_e)$$
$$+ \sum_{j=1}^{N_{\text{ions}}} m_{ej}\nu_{ej}\left[(\mathbf{v_e} - \mathbf{v_j})^2 + \frac{3}{m_j}(T_j - T_e)\right], \qquad (16)$$

where κ_e is the electron thermal conductivity. In addition, to running the code in the kinetic ion mode described above, we have also run with Lagrangian fluid-ion particles, as described in Ref. 50. The fluid-ion drift momentum the push is described by Eq. (15) with self-scattering included via an ion pressure gradient term, ∇P_k, and inter-particle collisions are treated via a fluid scattering model.[34] In this fluid-ion mode, the ion temperature is evolved via an energy equation similar to Eq. (16). Fusion is included in the simulations via pairwise binary sampling of the deuterons, reaction products are calculated in the center-of-mass frame of reference and then transformed back into the laboratory frame.[51] In the fluid ion case, each fluid ion particle is split into 10 sub-particles that randomly sample the thermal velocity based on the fluid temperature and then fusion is performed on the sub-particles via the same method as with kinetic ions. The simulations were run in 2D RZ cylindrical geometry with a box size of 6 mm in z and 10 mm in r using 100 μm cell size in both dimensions. The time step in the simulations was $\sim$200 fs. The time step is small enough to resolve the ion-ion collision frequency across the interpenetrating plasma; this may not necessarily be small enough to resolve this frequency in the cold solid target, though for neutron generation this region is of less interest. We did convergence tests down to cell sizes of 25 μm and found that these gave the same results. The simulations were initialized with 1600 ion macro-particles per species per cell in both the kinetic-ion and the fluid-ion cases.

B. Plasma parameters of the simulations

To understand the plasma parameters inferred via the NTOF measurements, we studied the temporal evolution of the deuteron flow velocity, electron density, and deuteron temperature in the center of the two foils as shown in Fig. 5 for both the kinetic-ion (solid curves) and fluid-ion (dashed curves) simulations. As we are interested in understanding these parameters with respect to the neutrons, we plot the neutron production rate in Figs. 5(a) and 5(e). We highlight the time of peak neutron production in the kinetic simulations using a solid vertical line and the time that the center 60% of neutrons are produced as a gray background.

In the CD/CD case, we find that the flow velocity is consistent with the NTOF measurements; flow velocities are around 500 km/s during the time of peak neutron production. The temperatures in both cases, 4–7.5 keV, are also similar to the inferred values from the NTOF measurements. In corroboration of previous work by Rambo and Procassini,[33] we find agreement between the kinetic-ion and fluid-ion treatments in terms of electron density and ion temperature. We find fairly good agreement with ion velocity, though the fluid simulations are slower at late times. This difference in velocity causes the neutron production rate to be lower in the fluid-ion case, though the relative shapes of the both cases are similar.
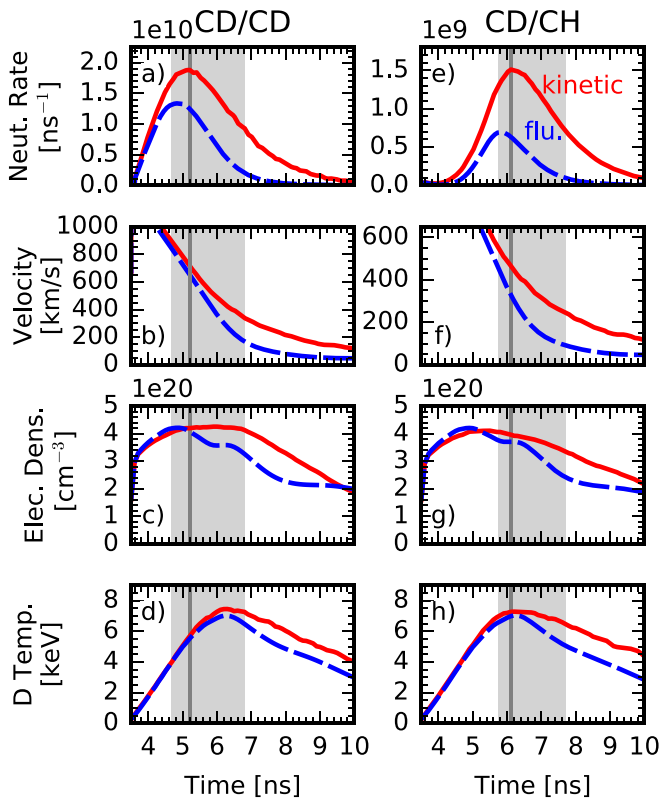
FIG. 5. Results from the hd-PIC CD/CD simulations: (a) neutron production rate of the entire plasma, (b) deuteron velocity, (c) electron density, and (d) deuteron temperature at the mid-point between the two foils. Panels (e)–(h) represent the same values as (a)–(d) but for the CD/CH case. Solid and dashed curves represent the kinetic-ion and fluid-ion simulations, respectively. The time of peak neutron production in the kinetic simulations is shown using a solid vertical line and the time that the center 60% of neutrons are produced is shown as a gray background.

In the CD/CH case, we find that the ion flow velocity of around 500 km/s is much higher than the velocity inferred via the multi-fluid method (i.e., 82 km/s). Even in the fluid case, the ion velocity is always greater than 100 km/s when the peak 60% of neutrons are being produced. There is slightly lower effective velocity in the CD/CH case compared to CD/CD due to the fact that neutrons are produced later in time. However, the large discrepancy in the inferred velocity (using a multi-fluid description) between CD/CD and CD/CH cases is not resolved via the difference in temporal production of neutrons alone.

To understand the collisionality of the two streams, we look at the collision rate and the collisional mean-free-path for carbon-carbon collisions. We look at this from two perspectives as described via a fluid scattering model by Jones *et al.*[34] The first is the rate of momentum exchange between the two streams, ν, Eq. (7) in Ref. [34], related to the relative velocity, v_{rel}, of the two streams. The second is the rate of energy/temperature exchange, ν^ϵ, Eq. (8) in Ref. [34], related to the thermal speed, v_{th}, of the streams. Related to these are the mean-free-paths for momentum, $\lambda = v_{rel}/\nu$, and for energy exchange, $\lambda^\epsilon = v_{th}/\nu^\epsilon$. These are both plotted in Fig. 6, with the solid and dashed curves
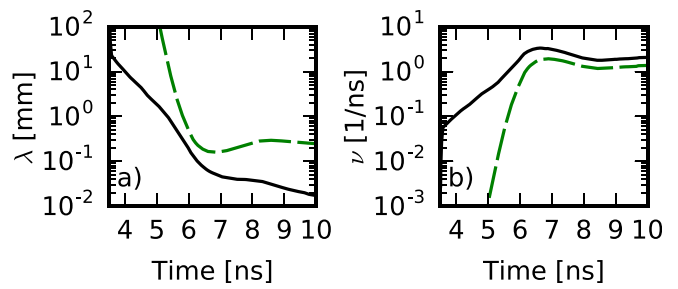

FIG. 6. (a) Plots of the mean-free-path and (b) the collision rate versus time for carbon-carbon collisions. The solid curves represent momentum exchange and the dashed curves represent energy exchange.

representing momentum-exchange and energy-exchange, respectively. These plots show a system rapidly changing in time. We see that the momentum-exchange mean-free-path varies from 5 mm to 0.3 mm over the time that most of the neutrons are being produced. These values can be compared to a system size of 6 mm that is on this same order of magnitude.

C. Synthetic diagnostic results

Of interest to our study are the fusion neutrons generated by the interaction of the interpenetrating flows. In Fig. 7, we show the spatial distribution of the neutron emission in both the CD/CD and CD/CH cases. As we expected from the experimental observations, the majority of neutrons originate from the center region between the two foils, indicating that they are produced by the interaction of the flows.

To directly compare neutrons produced in the simulation with neutrons observed on the NTOFs, we produce a synthetic NTOF signal using neutrons emitted in the appropriate angle of the detectors, the neutrons propagate the appropriate distance to arrive at the detector and we take into account the temporal and energy responses of the detectors (see Appendix A). These signals are plotted in Fig. 8 where we have normalized the
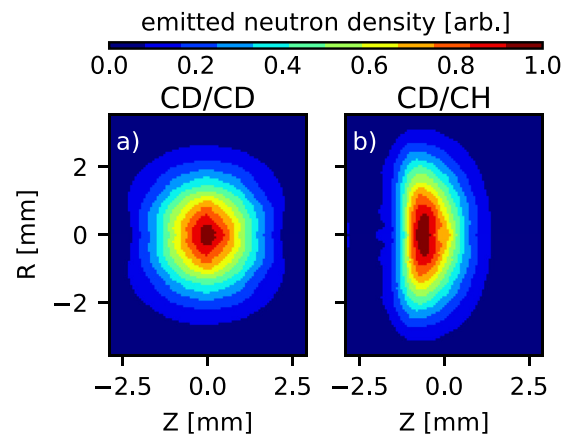

FIG. 7. Pseudo-color contours of the spatial density of the neutron emission from the kinetic-ion simulations for (a) CD/CD and (b) CD/CH, where the CH foil is on the right side. The plot is mirrored around the R-axis for clarity.
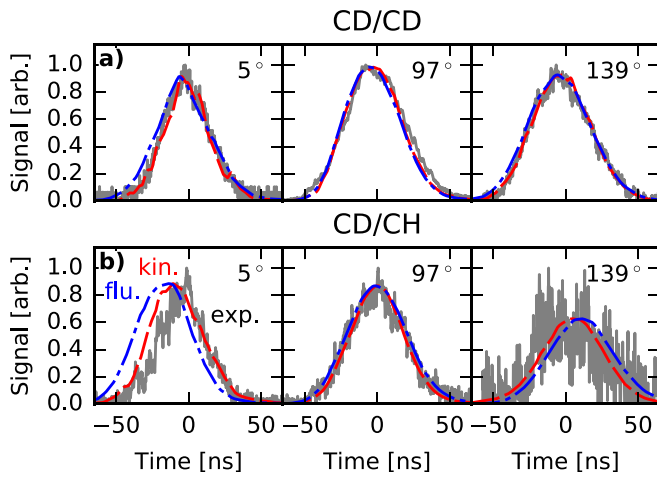
FIG. 8. Normalized synthetic NTOF signals for the kinetic-ion (dashed lines) and fluid-ion (dashed-dotted lines) hd-PIC simulations plotted against the experimental signals. Panel (a) shows the CD/CD case and panel (b) the CD/CH case. Time zero corresponds to a neutron of 2.45 MeV arriving at the detector.

simulations to match the experimental data, though we note that, by design, in the CD/CD kinetic case the total neutron yield is the same as in experiments. The synthetic NTOF diagnostics are plotted in Fig. 8, where the experimental data are replotted (solid curves) along with the synthetic signals from the kinetic-ion (dashed curves) and fluid-ion (dash-dotted curves) hd-PIC simulations. As expected, we find that both the kinetic-ion and fluid-ion simulations agree well with the experimental data in the CD/CD case. The reason for this is that the neutron generation is dominated by beam-beam fusion and is thus relatively insensitive to the exact distribution function of the reacting deuterons. However, we see that neither simulation is able to completely capture the NTOF data in the CD/CH case. We illustrate the differences in the neutron mean velocity in Fig. 9 via the same method used to create Fig. 4. Again, these illustrate good agreement in the CD/CD case, but poor agreement for CD/CH. Fitting the simulations using Eq. (7), we find that the
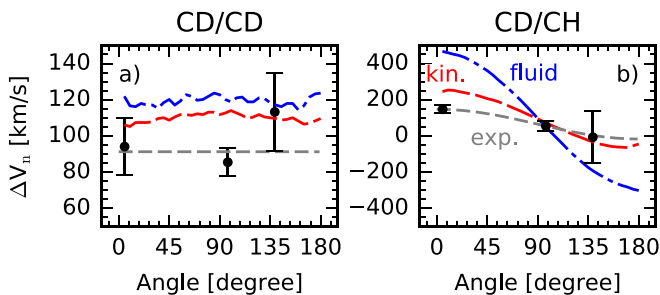

FIG. 9. Neutron mean velocity as a function of angle for the (a) CD/CD and (b) CD/CH cases. The solid circles with error bars represent the experimental data, which are fit with the short dashed gray curve. The long dashed curve represents the kinetic ion simulation and the dashed-dotted curve represents the fluid-ion simulation. In the CD/CH case, the experiment is best fit with u_{cm} (u_{rel}) of 82 km/s (1941 km/s). The kinetic-ion and fluid-ion simulation are best fit with 160 km/s (2331 km/s) and 378 km/s (2338 km/s), respectively.

center-of-mass velocity u_{cm} is over-estimated in both the fluid-ion, $u_{cm} = 378$ km/s, and the kinetic-ion, $u_{cm} = 160$ km/s, with respect to the experimental value of 82 km/s. Interestingly, the kinetic-ion simulations are closer to the data, despite having a slightly higher ion velocity than the fluid simulations. As we will now show, the reason for this is that in the CD/CH case neutrons are produced within the CD flow via thermal-like neutron production. This type of neutron production is much more sensitive to the tails of the ion distribution and can be significantly modified by slight deviations from Maxwellian.

D. Effect of non-Maxwellian ions on neutron generation

To understand the details of the flow interpenetration, we focus on the CD/CH case. As our experimental results are all weighted by the neutron generation, we look at the time of peak neutron production, 6.2 ns in the CD/CH case and plot the z-velocity distribution functions of deuteron in Fig. 10(a). We plot kinetic-ion results as solid lines and fit a 1D Maxwell-Boltzmann (MB) distribution, $g(v_z)$, as a grey background

$$g(v_z) = \sqrt{\frac{m_D}{2\pi T}} \exp\left[-\frac{m_D}{2T}(v_z - \bar{v}_z)^2\right]. \quad (17)$$

The MB distribution is fit by matching the mean flow velocity, $\bar{v}_{1D}$, of 475 km/s

$$\bar{v}_{1D} = \int_{-\infty}^{\infty} k(v_z) v_z dv_z, \quad (18)$$

where $k(v_z)$ is the normalized 1D velocity distribution from the kinetic-ion simulations, and by matching the one-dimensional temperature, T, this was found to be 8.2 keV
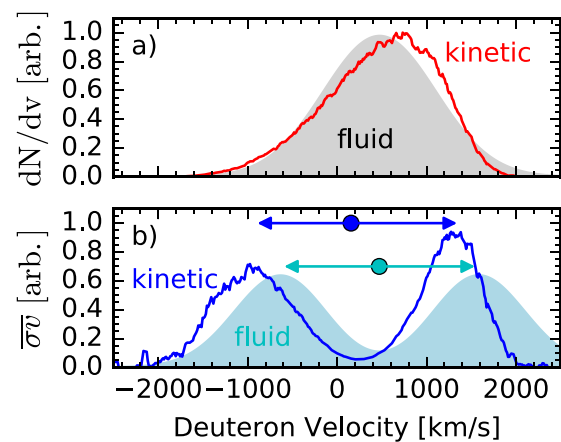
FIG. 10. (a) The 1D z-velocity distribution function of the deuterons from the kinetic-ion simulation (solid curve) in the CD/CH case at the time of peak neutron production rate, 6.2 ns, at the mid-plane between the foils ($z \pm 0.5$ mm, $r \pm 2$ mm). The 1D fluid MB fit (light background) is found using a velocity of $\bar{v}_{1D} = 475$ km/s and a 1D temperature of 8.2 keV. (b) Plot of $\overline{\sigma v}$ [see Eq. (21)] for the kinetic-ion simulation (solid line) and MB fit (light background). The neutron weighted deuteron velocities, $u_{cm,1D}$, are 470 km/s in the fluid-ion and 155 km/s in the kinetic-ion simulation; these are shown as solid circles on the plot.

$$T = m_D \int_{-\infty}^{\infty} k(v_z)(v_z - \bar{v}_z)^2 dv_z, \tag{19}$$

where m_D is the deuteron mass. We note that this velocity of $\bar{v}_{1D} = 475$ km/s is using a 1D fit for a snapshot in time at 6.2 ns and is used to provide a relevant example. It is clear from Fig. 10(a) that the kinetic distribution is skewed towards lower energy as compared to the MB fit. This skew is due to the fact that the scattering frequency is strongly inversely related to the relative velocity of the ions. Thus, ions that are moving slightly slower due to thermal variation in the flow are more strongly scattered than those moving at higher relative velocity to the opposing flow.

To understand how the ion distributions affect the neutron production, we integrate the neutron production rate. The result is a quantity that we denote as $\overline{\sigma v}$

$$\overline{\sigma v}(v) = f(v) \int_{-\infty}^{\infty} f(v_i)|v - v_i|\sigma(v - v_i)dv_i, \tag{20}$$

where σ is the cross-section for d(D,^{3}He)n reactions,[52] v_i is the velocity that is being integrated over, and $f(v)$ is the velocity distribution function. We note that, for simplicity in the plot, we have performed this as a 1D calculation; the full 3D calculation is included in the simulations. The function $\overline{\sigma v}$ tells us where in velocity space the neutrons are being produced and are shown in Fig. 10(b), where, again, the solid line is from the kinetic distribution and the fill is from the MB fit. In both the kinetic simulations and MB fit, we see double peaked functions as expected from a drifting quasi-thermonuclear plasma (e.g., Appendix B 4). These peaks correspond to the so-called Gamow peak[53] and are a consequence of the strong increase in σ with relative ion velocity, while on the other hand, the decay of the distribution function at higher relative ion velocities. We find that these peaks are significantly shifted to a lower velocity in the kinetic case as compared to the MB fit. This indicates that the mean velocity of the produced neutrons will also be downshifted, as observed in the synthetic data. To quantify this shift, we compute the neutron weighted velocity, which we call the 1D center-of-mass velocity, $u_{cm,1D}$, to be consistent with our previous terminology

$$u_{cm,1D} = \int_{-\infty}^{\infty} \overline{\sigma v}(v_z) \times v_z dv_z. \tag{21}$$

We find that the weighted velocity of the fluid MB fit, $u_{cm,1D}$, is almost identical to the mean velocity of the flow of $\bar{v}_{1D} = 475$ km/s, while the mean velocity of the kinetic-ion simulations is downshifted to $u_{cm,1D} = 155$ km/s, a factor of 3 difference in center-of-mass velocity. This is a large shift, especially considering that the skew of the distribution function [see Fig. 10(a)] does not seem drastically different that the MB fit based on the ion velocity alone.

We have used a snapshot in time and in 1D to analytically illustrate how the skew of the ion distribution can dramatically alter the velocity of neutrons produced. This effect is included intrinsically in the full kinetic-ion simulations that use a 3D ion distribution function and integrate the neutron production over all time. It is this skew effect that causes the kinetic-ion

simulations to produce a neutron-weighted center-of-mass velocity, u_{cm}, of only 160 km/s in the CD/CH case compared with 378 km/s from the fluid-ion simulations. However, this velocity is still higher than that observed experimentally by around a factor of 2. This observation, in addition to the discrepancy between the measured neutron yield reported previously,[12] is consistent with additional stopping effects due to collisionless electromagnetic instabilities that further skew the ion velocity distribution, such as the Weibel-filamentation instability[4] that has been previously observed on similar experiments.[11]

IV. SUMMARY

We have used experimental neutron time-of-flight (NTOF) measurements to evaluate the ion velocities and temperatures between two interpenetrating plasma flows from opposing targets of either CD/CD or CD/CH. Using a multi-fluid model to interpret the NTOF data in the CD/CD case, we find a flow velocity of 470 km/s for each flow, which is in reasonable agreement with other diagnostics. On the other hand, we find that using a multi-fluid approximation in the CD/CH case is not justified and gives unreasonable estimates of flow velocity. We find that this discrepancy is due, in part, to non-Maxwellian behavior in the CD plasma; as the deuterium in the CD stream is heated by collisions with the opposing flow it develops a skew towards lower energies.

This is modeled using a hydrodynamic-PIC model that includes collisions and electric fields, but does not include inertial electrons or magnetic fields. Using the code, we observe this non-Maxwellian skew due to collisions and thus a shift of the neutrons to lower a velocity. However, this does not fully account for the slower neutron velocities observed experimentally; the simulations are higher by around a factor of 2. This suggests that there is another source that slows or increases the skew of the ion distributions towards lower velocities. It seems reasonable that this is a signature of heating via the Weibel-filamentation instability as such instabilities have been observed experimentally[10,11] and are thought to be the cause for increased neutron yield.[12] Also, previous simulations of relativistic Weibel-mediated shocks show non-Maxwellian features.[54] We hope that future work will investigate the effects of such ion distribution modifications in these non-relativistic setups to better understand their effect on neutron generation. We believe that the methodology used in this work can also be applied to many issues relevant to inertial confinement fusion such as neutron yield anomalies in laser-driven capsule implosions,[22–24] interpenetration in the hohlraum[19–21] and converging fusion-plasma flows.[25–29]

ACKNOWLEDGMENTS

NOMENCLATURE

$\mathbf{u_{cm}}$	Center-of-mass velocity in a binary fusion reaction and as a fusion-weighted peak in the multi-fluid calculation
u_{rel}	Relative velocity in a binary fusion reaction and as a fusion-weighted peak in the multi-fluid calculation
T	Ion temperature of a multi-fluid flow
$\mathbf{v_f}$	Flow velocity of each individual multi-fluid flow
v_G	Velocity associated with the Gamow form of the fusion cross-section, see Eqs. (B23) and (B24)
V_0	Fusion neutron velocity magnitude in the absence of relative or center-of-mass velocity, see Eq. (B8)
$\mathbf{V_n}$	Fusion neutron velocity
$\Delta\mathbf{V_n}$	Fusion neutron velocity shift, $\mathbf{V_n} - V_0$

APPENDIX A: NEUTRON TIME-OF-FLIGHT RESPONSE FUNCTIONS

The temporal instrument response function of the NTOFs is shown in Fig. 11(a). Considering signal levels of $>10\%$ to be of relevance, we find that the width of the detector response is 9.8 ns. The energy dependent instrument response function of the NTOFs is shown in Fig. 11(b). In our experiment, we are focused on DD reactions ($Q = 3.27$ MeV); thus, for a cold, stationary DD plasma, the neutron production energy is 2.45 MeV, which corresponds to a neutron velocity of 21.65 Mm/s. Based on the neutron energies observed in our
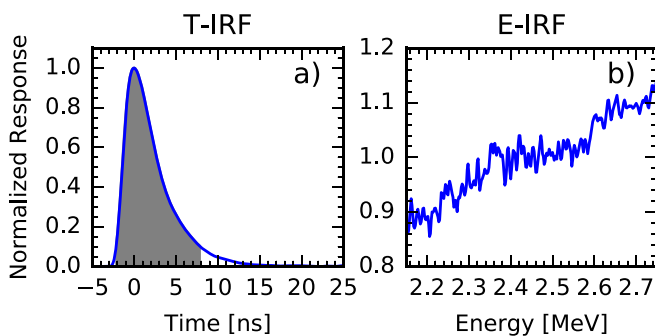

FIG. 11. (a) Normalized temporal instrument response function of the NTOF detectors. The solid line represents the IRF of the detectors. The filled in line corresponds to what we include as the uncertainty in detection, which we quantify as 10% of the peak. These values come at 2.1 and 7.8 ns prior and after the peak, respectively, meaning a total uncertainty of 9.8 ns. (b) Energy instrument response function of the NTOF detectors normalized to the value at 2.45 MeV. The energy range shown is consistent with the entire energy range of neutrons seen in the experiment. Notice that the scale varies only by $\pm12\%$.

experiment (2.45 ± 0.3 MeV), the detector response is found to vary by only $\pm12\%$.

APPENDIX B: INFERRING ION VELOCITY AND TEMPERATURE FROM NEUTRON VELOCITY SHIFT

1. Resultant neutron energy

For generality, we consider a fusion reaction of $1 + 2 \rightarrow n + 4$ with a Q-value, Q. In our case, the reaction is $D + D \rightarrow n + He^3$ and $Q = 3.269$ MeV. We refer to the particle n as a neutron, but particles n and 4 can be any products in the two body reaction. For ease of calculation, we use rest mass energies, which we signify with a "hat," as $\hat{m} = mc^2$, where m is the mass (e.g., in grams) and c is the speed of light. We follow treatments from previous works,[55,56] but shortened to highlight the relevant portions to our study. The relative velocity, $\mathbf{u}_{rel}$, of the two reactants is

$$\mathbf{u}_{rel} = \mathbf{u}_1 - \mathbf{u}_2, \tag{B1}$$

their center-of-mass velocity, $\mathbf{u}_{cm}$, is

$$\mathbf{u}_{cm} = \frac{\hat{m}_1\mathbf{u}_1 + \hat{m}_2\mathbf{u}_2}{\hat{m}_1 + \hat{m}_2}, \tag{B2}$$

and the magnitude of the velocity of the product n in the center-of-mass frame, V'_n, is

$$V'_n = \sqrt{\frac{2c^2}{\hat{m}_\star}(Q + E_r)}, \tag{B3}$$

where E_r is the kinetic energy in the center-of-mass frame

$$E_r = \frac{\hat{m}_r}{2}\frac{u_{rel}^2}{c^2}, \tag{B4}$$

with $\hat{m}_r$ being the reduced mass

$$\hat{m}_r = \frac{\hat{m}_1\hat{m}_2}{\hat{m}_1 + \hat{m}_2} \overset{DD}{\simeq} 937.8 \text{ MeV} \tag{B5}$$

and

$$\hat{m}_\star = \frac{\hat{m}_n}{\hat{m}_4}(\hat{m}_n + \hat{m}_4) \overset{DD}{\simeq} 1253.8 \text{ MeV}. \tag{B6}$$

The final neutron velocity is found by transforming back into the laboratory frame

$$\mathbf{V}_n = \mathbf{u}_{cm} + \mathbf{V}'_n. \tag{B7}$$

We define, V_0, as the velocity of the product n in the absence of relative (i.e., $\mathbf{v}_{rel} = 0$, $E_r = 0$) or center-of-mass velocity (i.e., $\mathbf{v}_{cm} = 0$). From (B3) and (B7), one sees that

$$V_0 = c\sqrt{\frac{2Q}{\hat{m}_\star}} \quad \overset{DD}{\simeq} 21.648 \times 10^3 \text{ km/s}. \tag{B8}$$

Of interest to us here is the magnitude of velocity of the neutron in an angle in the laboratory frame, θ. From (B3) and (B7), this is found to be

$$V_n = u_{cm}\cos\theta \pm \sqrt{V_0^2 + \frac{\hat{m}_r}{\hat{m}_\star}u_{rel}^2 - u_{cm}^2\sin^2\theta}, \qquad (B9)$$

where if $V_n' > v_{cm}$, as in our present work, then the positive root is taken.[55] To find the shift in neutron velocity, $\Delta V_n \equiv V_n - V_0$, we Taylor expand, with the consideration that V_0^2 is much greater than both v_{cm}^2 and $\frac{\hat{m}_r}{\hat{m}_\star}v_r^2 \simeq 0.748 v_{rel}^2$. We note that for the DD reactions this is valid to 1% up to around 2500 km/s and thus this will be true for our study.

$$\Delta V_n \simeq u_{cm}\left(\cos\theta - \frac{u_{cm}}{2V_0}\sin^2\theta\right) + \frac{1}{2V_0}\frac{\hat{m}_r}{\hat{m}_\star}u_{rel}^2. \qquad (B10)$$

Finally, we can assume that $2V_0 \gg u_{cm}$, which should be true up to 1% for center-of-mass velocities below 500 km/s and is also true in our study.

$$\Delta V_n \simeq u_{cm}\cos\theta + \frac{1}{2V_0}\frac{\hat{m}_r}{\hat{m}_\star}u_{rel}^2. \qquad (B11)$$

We note that for this work, we have used the full equation, (B9), exclusively for completeness. We show the previous simplifications to clarify the form of the equation for the reader.

2. Gamow peak of a beam-beam plasma

We begin with the general case of a two interpenetrating, drifting Maxwellian plasmas, f_+ and f_-, of the same ion species with the same ion temperature, T_i, number density, n_i, and that are drifting with a flow velocity, $\mathbf{v_f}$, directly opposing each other

$$f_\pm(\mathbf{v_i}) = \left(\frac{\hat{m}_i}{2\pi c^2 T_i}\right)^{\frac{3}{2}}\exp\left(-\frac{\hat{m}_i}{2c^2 T_i}(\mathbf{v_i}\pm\mathbf{v_f})^2\right). \qquad (B12)$$

We are interested in both how the plasmas interact with each other and themselves, so we add them together, renormalize, and call the distribution f_i

$$f_i(v_i) = \left(\frac{\hat{m}_i}{2\pi c^2 T_i}\right)^{\frac{3}{2}}\frac{1}{2}\left[\exp\left(-\frac{\hat{m}_i}{2c^2 T_i}(\mathbf{v_i}-\mathbf{v_f})^2\right)\right.$$
$$\left. + \exp\left(-\frac{\hat{m}_i}{2c^2 T_i}(\mathbf{v_i}+\mathbf{v_f})^2\right)\right]. \qquad (B13)$$

The number of reactions per unit time per unit volume with the cross section, σ, is

$$\frac{R_{12}(\mathbf{v_1},\mathbf{v_2})}{d^3\mathbf{v_1}d^3\mathbf{v_2}} = \frac{n^2}{2}v_r\sigma(v_r)f_i(\mathbf{v_1})f_i(\mathbf{v_2}). \qquad (B14)$$

We use the relative velocity, $\mathbf{v_{rel}}$, and center-of-mass velocity, $\mathbf{v_{cm}}$, to transform $\mathbf{v_1}$ and $\mathbf{v_2}$, where, for DD, $\hat{m}_1 = \hat{m}_2$ so $\hat{m}_r = \frac{1}{2}\hat{m}_1$

$$\mathbf{v_1} = \mathbf{v_{cm}} + \frac{1}{2}\mathbf{v_{rel}},$$
$$\mathbf{v_2} = \mathbf{v_{cm}} - \frac{1}{2}\mathbf{v_{rel}}. \qquad (B15)$$

This allows us to expand $(\mathbf{v_i}\pm\mathbf{v_f})^2$ as

$$(\mathbf{v_i}\pm\mathbf{v_f})^2 = \left(\mathbf{v_{cm}}\pm\frac{1}{2}\mathbf{v_{rel}}\pm\mathbf{v_f}\right)^2$$
$$= v_f^2 + v_{cm}^2 + \frac{1}{4}v_r^2 \pm\mathbf{v_{rel}}\cdot\mathbf{v_{cm}}$$
$$\pm 2\mathbf{v_f}\cdot\mathbf{v_{cm}}\pm\mathbf{v_f}\cdot\mathbf{v_{rel}}. \qquad (B16)$$

Therefore, designating the function $h_i(\mathbf{v_i})$ for simplicity

$$h_i(\mathbf{v_i}) = \exp\left([\mathbf{v_i}+\mathbf{v_f}]^2\right) + \exp\left([\mathbf{v_i}-\mathbf{v_f}]^2\right)$$
$$= \exp\left(v_f^2 + v_{cm}^2 + \frac{1}{4}v_r^2 \pm\mathbf{v_{rel}}\cdot\mathbf{v_{cm}}\right)$$
$$\times [\exp\left(2\mathbf{v_f}\cdot\mathbf{v_{cm}}\pm\mathbf{v_f}\cdot\mathbf{v_{rel}}\right) + \exp\left(-2\mathbf{v_f}\cdot\mathbf{v_{cm}}\mp\mathbf{v_f}\cdot\mathbf{v_{rel}}\right)]. \qquad (B17)$$

We then take $h_i(\mathbf{v_i})$ for $\mathbf{v_1}$ and $\mathbf{v_2}$ and multiply. We see that the $\pm\mathbf{v_{rel}}\cdot\mathbf{v_{cm}}$ term cancels and we get

$$h_i(\mathbf{v_1})h_i(\mathbf{v_2}) = \exp\left(2v_f^2 + 2v_{cm}^2 + \frac{1}{2}v_{rel}^2\right)$$
$$\times [\exp\left(4\mathbf{v_f}\cdot\mathbf{v_{cm}}\right) + \exp\left(2\mathbf{v_f}\cdot\mathbf{v_{rel}}\right)$$
$$+ \exp\left(-4\mathbf{v_f}\cdot\mathbf{v_{cm}}\right) + \exp\left(-2\mathbf{v_f}\cdot\mathbf{v_{rel}}\right)]. \qquad (B18)$$

We then take into account the definition of the hyperbolic cosine, $2\cosh(x) = e^x + e^{-x}$, and use these equation to get the reaction rate

$$\frac{R_{12}(\mathbf{v_{cm}},\mathbf{v_{rel}})}{d^3\mathbf{v_{cm}}d^3\mathbf{v_{rel}}} = \frac{n^2 v_{rel}\sigma(v_{rel})}{4}\left(\frac{\hat{m}_i}{2\pi c^2 T}\right)^3$$
$$\times \exp\left[-\frac{\hat{m}_i}{c^2 T}\left(v_f^2 + v_{cm}^2 + \frac{1}{4}v_{rel}^2\right)\right]$$
$$\times \left[\cosh\left(\frac{2\hat{m}_i}{c^2 T}\mathbf{v_f}\cdot\mathbf{v_{cm}}\right) + \cosh\left(\frac{\hat{m}_i}{c^2 T}\mathbf{v_f}\cdot\mathbf{v_{rel}}\right)\right]. \qquad (B19)$$

We can use the integration in Appelbe and Chittenden[56] Eq. (20)

$$\iiint f(\mathbf{v_k}\cdot\mathbf{v_j})d^3\mathbf{v_k} = 2\pi\int v_k^2\left[\int_{-1}^{1} f(v_k v_j x)dx\right]dv_k. \qquad (B20)$$

And given $\int_{-1}^{1}\cosh(-\alpha x)dx = (2/\alpha)\sinh(\alpha)$

$$\frac{R_{12}(v_{cm},v_{rel})}{dv_{cm}dv_{rel}} = \frac{n^2 v_{rel}\sigma(v_{rel})}{4v_f}\left(\frac{\hat{m}_i}{2\pi c^2 T}\right)^3$$
$$\times \exp\left[-\frac{\hat{m}_i}{c^2 T}\left(v_f^2 + v_{cm}^2 + \frac{1}{4}v_{rel}^2\right)\right]$$
$$\times \left[v_{cm}\sinh\left(\frac{2\hat{m}_i}{c^2 T}v_f v_{cm}\right) + 2v_{rel}\sinh\left(\frac{\hat{m}_i}{c^2 T}v_f v_{rel}\right)\right]. \qquad (B21)$$

The hyperbolic sine, $\sinh x$, has a very strong dependence on x. In our study, we expect that the largest velocity will be v_{rel}. This allows us to eliminate the $v_f v_{cm}$ term and, as v_{rel} is relatively large, we take $\sinh x \simeq \exp x$. We also integrate over v_{cm} (i.e., $\int_0^\infty \exp(-ax^2) = \sqrt{\pi/(4a)}$) and get the following:

$$\frac{R_{12}(v_{rel})}{dv_{rel}} = \frac{n^2}{8\sqrt{2}v_f}\left(\frac{\hat{m}_i}{2\pi c^2 T}\right)^{\frac{1}{2}} v_{rel}^2 \sigma(v_{rel})$$

$$\times \exp\left[-\frac{\hat{m}_i}{c^2 T}\left(v_f^2 + \frac{1}{4}v_{rel}^2 - v_f v_{rel}\right)\right]. \qquad (B22)$$

We include the cross-sectional dependence, where we use the Gamow form, written here as a function of velocity

$$\sigma(v_{rel}) = \frac{2c^2 S(E_r)}{\hat{m}_r v_{rel}^2}\exp\left(-\frac{v_G}{v_{rel}}\right), \qquad (B23)$$

where

$$v_G = \sqrt{\frac{2\epsilon_G}{m_r}} = 2\pi c\alpha_f Z_1 Z_2$$

$$\stackrel{DD}{\simeq} 13.74 \times 10^3 \text{ km/s}. \qquad (B24)$$

$S(E_r)$ is the astrophysical S-factor [$S(0) \simeq 54$ keV $\times$ barn for D(d,n)^{3}He], ϵ_G is the Gamow energy, α_f is the fine structure constant, and Z_1/Z_2 are the charge states of the reactant ions. We note that the Gamow form is most relevant for nonresonant reactions such as DD and should be used with caution with resonant reactions (e.g., DT, D^{3}He) due to the strong dependence of $S(E_r)$ with energy in these cases.[53]

The final form of the reaction rate per volume is

$$\frac{R_{12}(v_{rel})}{dv_{rel}} = \frac{n^2 c^2 S(E_r)}{2\sqrt{2}\hat{m}_i v_f}\left(\frac{m}{2\pi T}\right)^{\frac{1}{2}}$$

$$\times \exp\left[-\frac{v_G}{v_{rel}} - \frac{\hat{m}_i}{c^2 T}\left(v_f^2 + \frac{1}{4}v_{rel}^2 - v_f v_{rel}\right)\right]. \qquad (B25)$$

The main purpose of this exercise was to find the so-called "Gamow peak" in velocity, u_{rel}, which is the peak relative velocity of the maximum neutron production rate. We can find this by finding the maximum of R_{12} as a function of v_r, which means taking the derivative and setting to zero

$$v_f = \frac{1}{2}\left(u_{rel} - \frac{2Tc^2 v_G}{\hat{m}_i u_{rel}^2}\right). \qquad (B26)$$

Unfortunately, this is a bit tricky to invert and solve for u_{rel}; while it is possible, it is very ugly. We can see quite nicely that it recovers the correct limits. For instance, in the stationary case $v_f = 0$, we recover the classical Gamow peak[53]

$$v_f = 0 : \quad u_{rel} = \left(\frac{Tc^2 v_G}{\hat{m}_i}\right)^{\frac{1}{3}}. \qquad (B27)$$

This is equivalent to $(m_r/2)u_{rel}^2 = T[\epsilon_G/(4T)]^{1/3}$. If we have no thermal spread $T = 0$, then we recover the beam-beam kinematic result

$$T = 0 : \quad u_{rel} = 2v_f. \qquad (B28)$$

3. Beam-beam fusion of interpenetrating hot plasmas

Let us first consider a case of two symmetric interpenetrating beams. In this case, we do not expect there to be any

center-of-mass velocity (i.e., $v_{cm} = 0$) as the beams are not flowing together. This is easily seen in the CD/CD data as there is no angular dependence on the velocity shift. Thus, to find u_{rel} in this case, we solve Eq. (B9) with the center-of-mass velocity set to zero to solve for u_{rel}

$$\text{Beam-Beam}: \quad \Delta V_n = -V_0 + \sqrt{V_0^2 + \frac{\hat{m}_r}{\hat{m}_\star}u_{rel}^2}$$

$$\simeq \frac{1}{2V_0}\frac{\hat{m}_r}{\hat{m}_\star}u_{rel}^2. \qquad (B29)$$

To determine the velocity of the convert u_{rel} into a flow velocity, we solve the following equation, from (B26), rewritten here to clarify the method:

$$\text{Beam-Beam}: \quad v_f = \frac{1}{2}\left(u_{rel} - \frac{2Tc^2 v_G}{\hat{m}_i u_{rel}^2}\right). \qquad (B30)$$

We note that this equation has two potential unknowns, v_f and T, and thus, in the beam-beam case, we need a way to constrain one of these two in order to determine the other. To illustrate these results, we find the neutron production rate as a function of velocity for a beam-beam plasma in 1D by integrating the equation

$$\overline{\sigma v}(v) = f(v)\int_{-\infty}^{\infty} f(v_i)|v - v_i|\sigma(v - v_i)dv_i, \qquad (B31)$$

where $f(v)$ is the beam-beam plasma distribution function in 1D

$$f(v) = \exp\left(-\frac{(v - v_f)^2}{2c^2 T/\hat{m}}\right) + \exp\left(-\frac{(v + v_f)^2}{2c^2 T/\hat{m}}\right), \qquad (B32)$$

with a flow velocity of 600 km/s and a temperature of 5 keV. We plot the normalized distribution function $f(v)$ and $\overline{\sigma v}(v)$ in Fig. 12. This plot illustrates how the Gamow peak is pushed outward in velocity both by the flow velocity and, also, by the temperature of the flows.

4. Thermonuclear fusion in a drifting plasma

The other case of interest is that of a drifting plasma that is producing neutrons via thermonuclear fusion. In this case, there is a center-of-mass velocity, which as it is traveling with
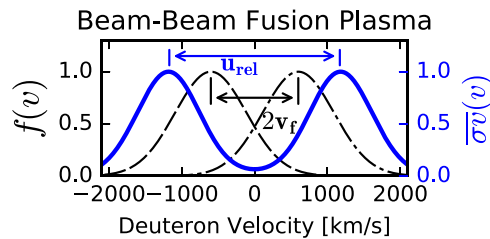

FIG. 12. Ion distribution function, $f(v)$, a sum of the dashed and dashed-dotted lines and $\overline{\sigma v}(v)$ as a thick solid line, for a beam-beam plasma with a flow velocity of 600 km/s and a temperature of 5 keV.
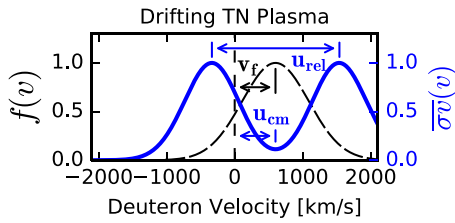
FIG. 13. Ion distribution function, $f(v)$, (dashed line) and $\overline{\sigma v}(v)$ (solid line) for a drifting thermonuclear plasma with a flow velocity of 600 km/s and a temperature of 5 keV.

the flow velocity, v_f, and this will be equal to the peak center-of-mass velocity, u_{cm}. Thus, from (B9), we get the following:

$$\text{TN Drift}: \quad \Delta V_n = -V_0 + u_{cm}\cos\theta$$
$$\pm\sqrt{V_0^2 + \frac{\hat{m}_r}{\hat{m}_\star}u_{rel}^2 - u_{cm}^2\sin^2\theta}$$
$$\simeq u_{cm}\cos\theta + \frac{1}{2V_0}\frac{\hat{m}_r}{\hat{m}_\star}u_{rel}^2, \tag{B33}$$

which gives us both the values u_{cm} and u_{rel}. To determine the temperature of the flow, we can then use (B26) with the flow velocity set to zero to give

$$\text{TN Drift}: \quad T = u_{rel}^3\frac{\hat{m}_i}{c^2 v_G}. \tag{B34}$$

Thus, we see in this case that we can solve for both the drift of the plasma and its temperature from the angularly resolved measurement of the neutron velocity shift. Again, we illustrate this by evaluating (B31), this time with then 1D drifting plasma distribution function

$$f(v) = \exp\left(-\frac{(v - v_f)^2}{2c^2 T/\hat{m}}\right), \tag{B35}$$

with a flow velocity of 600 km/s and a temperature of 5 keV. We plot these results in Fig. 13. We see in this case that the production peak is shifted by the flow velocity of the plasma and the spread of the peak, u_{rel}, is now completely determined by the temperature of the flow.

APPENDIX C: SENSITIVITY OF THE SIMULATION RESULTS TO THE VELOCITY MULTIPLIER

We simulation the first 3.5 ns of the interaction using the single-fluid radiation-hydrodynamic code HYDRA to model the laser ablation and plasma expansion. After this time, we switch the modeling to the hybrid-PIC code CHICAGO to that we can model the interpenetration. However, CHICAGO did not include the laser radiation, which in the experiment continued for 5 ns and thus we expect that the velocity will be artificially lower in CHICAGO than in experiment. For this reason, we have used velocity multipliers, M_v, to increase the velocity. Also, to match the total neutron yields in the CD/CD case, we increase the density. As a sanity check for the HYDRA

simulations, we show that the simulations are in agreement with self-similar expansion[57,58]

$$v = z/t + C_s, \tag{C1}$$

where v is the flow speed, z is the location, t is the time, and $C_s = \sqrt{\gamma Z T_e/m_i}$ is the sound speed with γ as the adiabatic constant, Z as the ionization state, T_e as the electron temperature, and m_i as the ion mass. We compare this model to HYDRA velocity profiles (solid curve) at $z = 3$ mm from the target surface in Fig. 14(a). As the electron temperature is changing in time, we plot use limits of 1 and 2 keV for the electron temperature to calculate the self-similar expansion (gray region). These bounds agree with the simulated electron temperature. In Fig. 14(b), we show a smaller time window and also plot the velocities from CHICAGO when directly using $M_v = 1$ (diamonds) and $M_v = 1.1$ (squares) velocity multiplier. Here, it is clear that the $M_v = 1$ case is always at a slower velocity than the HYDRA simulations. However, the $M_v = 1.1$ case is both above and below the HYDRA simulations; as we can see in this case the velocities are similar around 5 ns, where the neutron production rate is maximum in the CD/CD case. We clarify that all of these plots are in the case of a single foil of CD so that there is no interaction with an opposing plasma flow.

To understand the impact of the velocity multipliers on peak neutron velocity, we compared the simulations for CD/CD and CD/CH used in the main text, $M_v = 1.1$, to multipliers of $M_v = 1$ and $M_v = 1.2$. We plot neutron velocity shift ΔV_n for the CD/CD case in Fig. 15(a) where the simulations ($M_v = 1$ are diamonds, $M_v = 1.1$ are squares, $M_v = 1.2$ are triangles) are plotted against the experimental data (open circles). We also show the fits using Eq. (7) to the data and experiment in Table III. As expected, the higher velocity multipliers cause the neutron velocity to shift upwards due to the higher relative velocity between the flows. As compared to the experimental data, all of the simulated shifts are on the higher side of the error bars. Figure 15(b) shows the CD/CH case for the same selection of velocity multipliers. Here, we notice that with higher
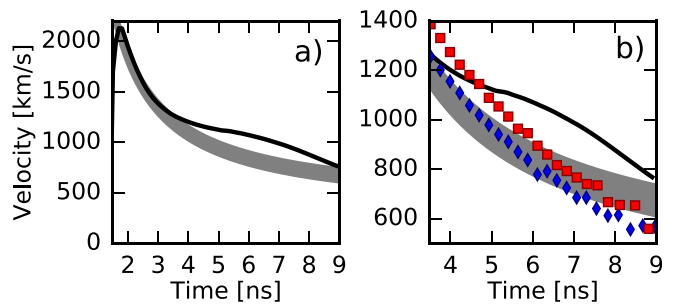

FIG. 14. Simulated ion velocity in the z-direction at 3 mm from the target surface from HYDRA (solid curve), the self-similar expansion model (gray region) from Eq. (C1) using limits of $C_s = 280$ and 400 km/s corresponding to electron temperatures of 1 and 2 keV, respectively, and CHICAGO simulations of a single CD target with a 1× (diamonds) and a 1.1× (squares) velocity multiplier. The two panels show the same data: (a) illustrates the agreement of HYDRA with self-similar expansion over a longer time period, and (b) shows a time window corresponding to the times of interest for the CHICAGO simulations.
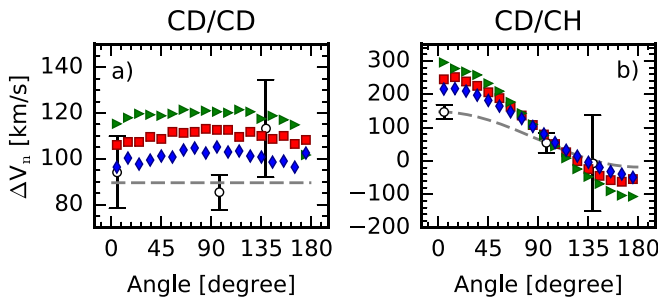
CD/CD

CD/CH

FIG. 15. Neutron velocity shifts in (a) the CD/CD and (b) the CD/CH cases. Experimental data are shown as open circles, with the dashed line representing the fit from Eq. (7). Simulations are shown as diamonds, squares and triangles, representing velocity multipliers of $M_v = 1.0$, $M_v = 1.1$, and $M_v = 1.2$, respectively.

TABLE III. Fits to the neutron shifts using the two-particle kinematic Eq. (7).

		Exp.	1.0×	1.1×	1.2×	
CD/CD	u_{rel}	2300	2420	2525	2615	km/s
CD/CH	u_{rel}	1941	2274	2332	2315	km/s
	u_{cm}	82	133	160	199	km/s

velocity multiplier a larger variation in the neutron velocity as expected from the higher center-of-mass velocity in this case. All of the simulated data over predict the experimental values. Thus, in both the CD/CD and CD/CH cases, we find that the neutron shifts are either in agreement or larger in magnitude than the experimental data. We can think of a few potential reasons for this: (1) the initial conditions are incorrect, (2) a mechanism not included in the simulations causes the flows to slow down or (3) in the CD/CH case, a mechanism not included in the simulations causes a stronger skew in the ion distributions than seen by collisional simulations alone.

In general, we have found that HYDRA is accurate and, in fact, relatively insensitive to laser parameters, in terms of the velocity of the flow. We have found across a variety of simulations that the expansion velocity generally follows a self-similar model, as illustrated in Fig. 14. This may not be true when the plasma is strongly radiative or the equation-of-state dominates the plasma dynamics, however these are relatively unimportant in an expanding CD plasma. Thus, we believe that our initial conditions are accurate. Therefore, the cause of the lower neutron velocities is likely a mechanism not included in our simulations. This could cause either slowing and/or skewing of the ion distribution to give the lower values of u_{cm} observed experimentally. Given the observation of magnetic filaments at similar plasma parameters,[10,11] the Weibel-filamentation instability is a strong candidate for these effects.

REFERENCES

[1]P. Ghavamian, J. Raymond, R. C. Smith, and P. Hartigan, Astrophys. J. **547**, 995 (2001).

[2]A. Bamba, R. Yamazaki, M. Ueno, and K. Koyama, Astrophys. J. **589**, 827 (2003).

[3]H.-S. Park, D. D. Ryutov, J. S. Ross, N. L. Kugland, S. H. Glenzer, C. Plechaty, S. M. Pollaine, B. A. Remington, A. Spitkovsky, L. Gargate et al., High Energy Density Phys. **8**, 38 (2012).

[4]E. S. Weibel, Phys. Rev. Lett. **2**, 83 (1959).

[5]D. Ryutov, R. P. Drake, J. Kane, E. Liang, B. A. Remington, and W. M. Wood-Vasey, Astrophys. J. **518**, 821 (1999).

[6]D. Ryutov, N. Kugland, H. Park, C. Plechaty, B. Remington, and J. Ross, Plasma Phys. Controlled Fusion **54**, 105021 (2012).

[7]D. D. Ryutov, Phys. Plasmas **25**, 100501 (2018).

[8]J. Ross, S. Glenzer, P. Amendt, R. Berger, L. Divol, N. Kugland, O. Landen, C. Plechaty, B. Remington, D. Ryutov et al., Phys. Plasmas **19**, 056501 (2012).

[9]J. Ross, H.-S. Park, R. Berger, L. Divol, N. Kugland, W. Rozmus, D. Ryutov, and S. Glenzer, Phys. Rev. Lett. **110**, 145005 (2013).

[10]W. Fox, G. Fiksel, A. Bhattacharjee, P.-Y. Chang, K. Germaschewski, S. Hu, and P. M. Nilson, Phys. Rev. Lett. **111**, 225002 (2013).

[11]C. M. Huntington, F. Fiuza, J. S. Ross, A. B. Zylstra, R. P. Drake, D. H. Froula, G. Gregori, N. L. Kugland, C. C. Kuranz, M. C. Levy et al., Nat. Phys. **11**, 173–176 (2015).

[12]J. S. Ross, D. P. Higginson, D. Ryutov, F. Fiuza, R. Hatarik, C. Huntington, D. H. Kalantar, A. Link, B. B. Pollock, B. A. Remington et al., Phys. Rev. Lett. **118**, 185003 (2017).

[13]D. D. Ryutov, F. Fiuza, C. M. Huntington, J. S. Ross, and H.-S. Park, Phys. Plasmas **21**, 032701 (2014).

[14]F. Fiuza, R. Fonseca, J. Tonge, W. Mori, and L. Silva, Phys. Rev. Lett. **108**, 235004 (2012).

[15]A. Stockem, F. Fiuza, A. Bret, R. A. Fonseca, and L. O. Silva, Sci. Rep. **4**, 3934 (2014).

[16]A. Bret, A. Stockem, R. Narayan, and L. O. Silva, Phys. Plasmas **21**, 072301 (2014).

[17]C. Ruyer, L. Gremillet, and G. Bonnaud, Phys. Plasmas **22**, 082107 (2015).

[18]H. G. Rinderknecht, P. A. Amendt, S. C. Wilks, and G. Collins, Plasma Phys. Controlled Fusion **60**, 064001 (2018).

[19]L. Berzak Hopkins, S. Le Pape, L. Divol, N. Meezan, A. Mackinnon, D. Ho, O. Jones, S. Khan, J. Milovich, J. Ross et al., Phys. Plasmas **22**, 056318 (2015).

[20]S. Le Pape, L. F. Berzak Hopkins, L. Divol, N. Meezan, D. Turnbull, A. J. Mackinnon, D. Ho, J. S. Ross, S. Khan, A. Pak et al., Phys. Plasmas **23**, 056311 (2016).

[21]L. Q. Shan, H. B. Cai, W. S. Zhang, Q. Tang, F. Zhang, Z. F. Song, B. Bi, F. J. Ge, J. B. Chen, D. X. Liu et al., Phys. Rev. Lett. **120**, 195001 (2018).

[22]J. R. Rygg, J. A. Frenje, C. K. Li, F. H. Séguin, R. D. Petrasso, J. A. Delettrez, V. Y. Glebov, V. N. Goncharov, D. D. Meyerhofer, S. P. Regan et al., Phys. Plasmas **13**, 052702 (2006).

[23]H. G. Rinderknecht, H. Sio, C. K. Li, A. B. Zylstra, M. J. Rosenberg, P. Amendt, J. Delettrez, C. Bellei, J. A. Frenje, M. G. Johnson et al., Phys. Rev. Lett. **112**, 135001 (2014).

[24]M. Rosenberg, H. G. Rinderknecht, N. M. Hoffman, P. A. Amendt, S. Atzeni, A. B. Zylstra, C. K. Li, F. H. Séguin, H. Sio, M. G. Johnson et al., Phys. Rev. Lett. **112**, 185001 (2014).

[25]H. Daido, M. Yamanaka, K. Mima, K. Nishihara, S. Nakai, Y. Kitagawa, E. Miura, C. Yamanaka, and A. Hasegawa, Appl. Phys. Lett. **51**, 2195 (1987).

[26]A. V. Bessarab, V. A. Gaidash, G. V. Dolgoleva, N. V. Zhidkov, V. M. Izgorodin, G. A. Kirillov, G. G. Kochemasov, A. V. Kunin, D. N. Litvin, V. M. Murugov et al., Zh. Eksp. Teor. Fiz. **102**, 1800 (1992).

[27]Y. Abe, A. Sunahara, S. Lee, T. Yanagawa, Z. Zhang, Y. Arikawa, A. Morace, T. Nagai, T. Ikenouchi, S. Tosaki et al., Appl. Phys. Lett. **111**, 233506 (2017).

[28]X. Zhang, J. Zhao, D. Yuan, C. Fu, J. Bao, L. Chen, J. He, L. Hou, L. Li, Y. Li et al., Phys. Rev. C **96**, 055801 (2017).

[29]G. Ren, J. Yan, J. Liu, K. Lan, Y. H. Chen, W. Y. Huo, Z. Fan, X. Zhang, J. Zheng, Z. Chen et al., Phys. Rev. Lett. **118**, 165001 (2017).

[30]R. L. Berger, J. R. Albritton, C. J. Randall, E. A. Williams, W. L. Kruer, A. B. Langdon, and C. J. Hanna, Phys. Fluids B **3**, 3 (1991).

[31]R. A. Bosch, R. L. Berger, B. H. Failor, N. D. Delamater, G. Charatis, and R. L. Kauffman, Phys. Fluids B **4**, 979 (1992).

[32]S. Pollaine, R. Berger, and C. Keane, Phys. Fluids B **4**, 989 (1992).

[33]P. W. Rambo and R. J. Procassini, Phys. Plasmas **2**, 3130 (1995).

[34]M. E. Jones, D. S. Lemons, R. J. Mason, V. A. Thomas, and D. Winske, J. Comp. Phys. **123**, 169 (1996).

[35]A. S. Wan, T. W. Barbee, R. Cauble, P. Celliers, L. B. Da Silva, J. C. Moreno, P. W. Rambo, G. F. Stone, J. E. Trebes, and F. Weber, Phys. Rev. E **55**, 6293 (1997).

[36]Z. A. Ali, V. Y. Glebov, M. Cruz, T. Duffy, C. Stoeckl, S. Roberts, T. C. Sangster, R. Tommasini, A. Throop, M. Moran *et al.*, Rev. Sci. Instrum. **79**, 10E527 (2008).

[37]V. Y. Glebov, T. C. Sangster, C. Stoeckl, J. P. Knauer, W. Theobald, K. L. Marshall, M. J. Shoup, T. Buczek, M. Cruz, T. Duffy *et al.*, Rev. Sci. Instrum. **81**, 10D325 (2010).

[38]C. Stoeckl, M. Cruz, V. Y. Glebov, J. P. Knauer, R. Lauck, K. Marshall, C. Mileham, T. C. Sangster, and W. Theobald, Rev. Sci. Instrum. **81**, 10D302 (2010).

[39]M. G. Johnson, J. A. Frenje, D. T. Casey, C. K. Li, F. H. Séguin, R. Petrasso, R. Ashabranner, R. M. Bionta, D. L. Bleuel, E. J. Bond *et al.*, Rev. Sci. Instrum. **83**, 10D308 (2012).

[40]H. G. Rinderknecht, M. G. Johnson, A. B. Zylstra, N. Sinenian, M. J. Rosenberg, J. A. Frenje, C. J. Waugh, C. K. Li, F. H. Sèguin, R. D. Petrasso *et al.*, Rev. Sci. Instrum. **83**, 10D902 (2012).

[41]H. Brysk, Plasma Phys. **15**, 611 (1973).

[42]L. Ballabio, J. Källne, and G. Gorini, Nucl. Fusion **38**, 1723 (1998).

[43]T. J. Murphy, Phys. Plasmas **21**, 072701 (2014).

[44]M. M. Marinak, G. D. Kerbel, N. A. Gentile, O. Jones, D. Munro, S. Pollaine, T. R. Dittrich, and S. W. Haan, Phys. Plasmas **8**, 2275 (2001).

[45]C. Thoma, D. R. Welch, R. E. Clark, D. V. Rose, and I. Golovkin, Phys. Plasmas **24**, 062707 (2017).

[46]A. Glocer, G. Tóth, Y. Ma, T. Gombosi, J.-C. Zhang, and L. Kistler, J. Geophys Res.: Space Phys. **114**, A12203, https://doi.org/10.1029/2009JA014418 (2009).

[47]K. Nanbu, Phys. Rev. E **55**, 4642 (1997); K. Nanbu, Phys. Rev. E **56**, 7314 (1997).

[48]K. Nanbu and S. Yonemura, J. Comput. Phys. **145**, 639 (1998).

[49]D. P. Higginson, J. Comput. Phys. **349**, 589 (2017).

[50]C. Thoma, D. R. Welch, R. E. Clark, N. Bruner, J. J. MacFarlane, and I. E. Golovkin, Phys. Plasmas **18**, 103507 (2011).

[51]D. P. Higginson, A. Link, and A. Schmidt, "A Pairwise Nuclear Fusion Algorithm for Weighted Particle-in-Cell Plasma Simulations," J. Comp. Phys. (unpublished).

[52]H. Bosch and G. M. Hale, Nucl. Fusion **32**, 611 (1992).

[53]S. Atzeni and J. Meyer-Ter-Vehn, *The Physics of Inertial Fusion* (Oxford Univesity Press, 2004).

[54]S. F. Martins, R. A. Fonseca, L. O. Silva, and W. B. Mori, Astrophys. J. Lett. **695**, L189 (2009).

[55]J. B. Ball, Technical Report No. ORNL-3251 (Oak Ridge National Laboratory, Tennessee, 1962).

[56]B. Appelbe and J. Chittenden, Plasma Phys. Controlled Fusion **53**, 045002 (2011).

[57]A. V. Gurevich, L. V. Pariiskaya, and L. P. Pitaevskii, Zh. Eksp. Teor. Fiz. **49**, 647 (1965) [Sov. Phys. JETP **22**, 449 (1966)].

[58]J. E. Crow, P. L. Auer, and J. E. Allen, J. Plasma Phys. **14**, 65 (1975).